

**Snapping of hinged arches under displacement control: Strength loss and nonreciprocity**Gabriele Librandi <sup>1</sup>, Eleonora Tubaldi <sup>2,\*</sup>, and Katia Bertoldi <sup>1,†</sup><sup>1</sup>*John A. Paulson School of Engineering and Applied Sciences, Harvard University, Cambridge, Massachusetts 02138, USA*<sup>2</sup>*Mechanical Engineering Department, University of Maryland, College Park, Maryland 20742, USA*

(Received 14 December 2019; accepted 6 April 2020; published 20 May 2020)

We investigate experimentally and numerically the response of hinged shallow arches subjected to a transverse midpoint displacement. We find that this simple system supports a rich set of responses, which, to date, have received relatively little attention. We observe not only the snapping of the arches to their inverted equilibrium configuration, but also an earlier dynamic transition from a symmetric to an asymmetric shape that results in a sudden strength loss. Moreover, we find that the response of plastically deformed arches is nonreciprocal with respect to the loading direction. Finally, we discover that, while elastically deformed arches always snap to the inverted stable configuration, for plastically deformed ones there is a critical rise below which the structures are monostable.

DOI: [10.1103/PhysRevE.101.053004](https://doi.org/10.1103/PhysRevE.101.053004)**I. INTRODUCTION**

While for thousands years arches have been used as structural elements capable of spanning large openings [1,2], more recently they have attracted significant interest because of their ability to snap between two stable configurations [3–8]. By controlling such snap-through instability scientists and engineers have designed a broad range of structures and devices across scales, including aerospace morphing systems [9], microelectromechanical (MEMS) devices [10,11], fluidic systems with passive control of viscous flow [12], energy-trapping structures [13], microactuators [14], switches [15], and metamaterials to manipulate the propagation of elastic pulses [16,17]. However, while in these innovative applications the arched elements are typically loaded by controlling their transverse displacement, most of previous efforts to accurately capture their snapping behavior have focused on the response induced by a fixed load [18–23].

Here we use a combination of experiments and analyses to investigate the response of a hinged arch subjected to a midpoint transverse displacement. To our surprise, we find that the behavior of this system is very rich and still unexplored. First, for a wide range of rises the system is characterized by a dynamic transition even before snapping. Such a transition manifests itself as a sudden force drop and corresponds to the instantaneous asymmetric reconfiguration of the arch. Second, the response of plastically deformed arches is nonreciprocal with respect to the loading direction, as the maximum recorded force and the snapping time are significantly different when the direction of the applied displacement is changed. Third, while elastically deformed arches snap for any rise, we discover a critical rise (i.e., critical snapping threshold) below which for plastically deformed arches snapping does not occur. Given all these interesting features, we envision

shallow arches to serve as building blocks for highly nonlinear metamaterials capable of manipulating the transmission of mechanical signals in unprecedented ways.

**II. EXPERIMENTS**

We start by experimentally investigating the response of two shallow arches with simply supported ends when subjected to a midpoint transverse displacement. The two arches have identical span,  $L = 120$  mm, and rise,  $e^{(1)} = 11$  mm [see inset in Fig. 1(c)]. Moreover, both arches are made of an initially flat spring steel shim of length  $L_0 = 122.5$  mm (note that this length includes also the hinges), but one is realized by plastically deforming it into the target shape  $e^{(1)} \sin(\pi x/L)$  [Fig. 1(a)], while the other one is fabricated by applying an axial force to elastically buckle it [Fig. 1(b); see also Supplemental Material, Fabrication section [24]]. As such, the plastically deformed arch permanently maintains the sinusoidal shape, while the elastically deformed one returns to its straight configuration as soon as removed from the hinges. We arrange the two arches so that they are initially curved upwards and conduct two tests on each of them using an indenter that moves their midpoints at a constant speed  $\alpha$ . In the first experiment (which we refer to as *Loading 1*) we apply a downward displacement  $d^{(1)} < 0$  to snap the arches to their inverted equilibrium configuration, while in the second one (which we refer to as *Loading 2*) we impose an upward midpoint displacement  $d^{(2)} > 0$  to the inverted arches to snap them back to their initial configuration (see Movie S1 and Fig. S5 [24]).

In Figs. 1(c) and 1(d) we show results for tests conducted at  $\alpha = 15$  mm/s and find that the response of our arches is characterized by three distinct regimes. First, the arches deform symmetrically and the force monotonically increases. Second, at  $t = t_{\text{asym}}$  they transition to an asymmetric shape [see snapshots in Figs. 1(e) and 1(f)]. Remarkably, this transition is a dynamic event that results in a sudden drop in force. Note that such a drop, to our best knowledge has

\*etubaldi@umd.edu

†bertoldi@seas.harvard.edu

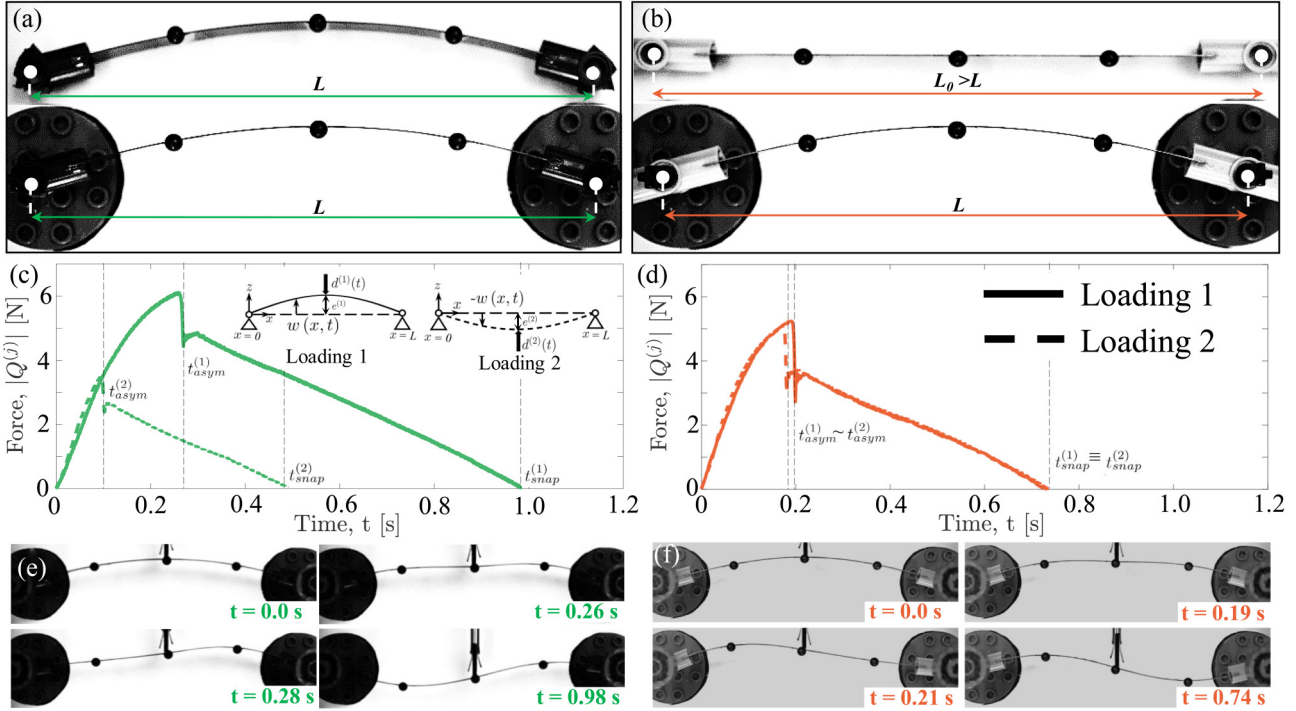


FIG. 1. (a)–(b) Snapshots of our (a) plastically deformed arch and (b) elastically deformed arch before and after mounting on the end supports. (c)–(d) Forces recorded during the tests for the (c) plastically and (d) elastically deformed shallow arches subjected to *Loading 1* (continuous lines) and *Loading 2* (dashed lines). (e)–(f) Snapshots of the (e) plastically and (f) elastically deformed shallow arches subjected to *Loading 1*.

never been observed in snapping experiments conducted on arches under displacement-controlled conditions, as it was prevented by either clamped boundary conditions [4] [see also Fig. S7 [24]] or loading offset [5] [see also Fig. 2(b)]. After this dynamic transition, the recorded force linearly

decreases until  $t = t_{\text{snap}}$ , when the arches snap to the inverted stable configuration. Surprisingly, while for the elastically deformed arch  $t_{\text{snap}}$  is identical for *Loading 1* and *Loading 2* (i.e.,  $t_{\text{snap}}^{(1)} = t_{\text{snap}}^{(2)}$ ), for the plastically deformed one it is very different for the two loading scenarios (i.e.,  $t_{\text{snap}}^{(1)}/t_{\text{snap}}^{(2)} \sim 1.98$ ;

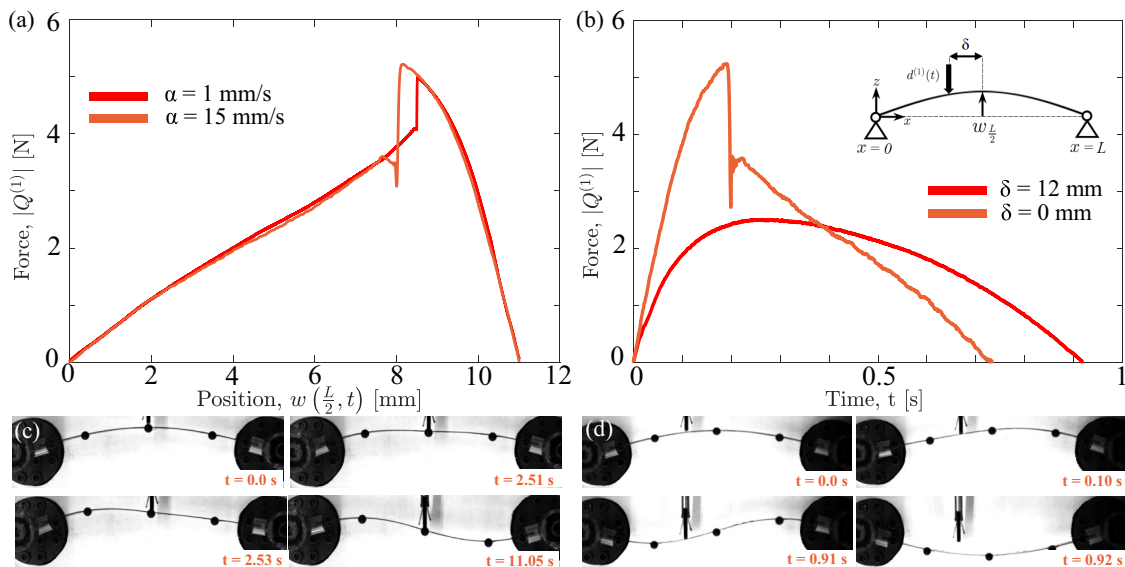


FIG. 2. (a)–(b) Forces recorded when indenting an elastically deformed arch according to *Loading 1* (a) at  $\alpha = 1$  and  $15$  mm/s and (b) with  $\delta = 0$  and  $12$  mm. (c)–(d) Snapshots of our elastically deformed arch when tested at (c)  $\alpha = 1$  mm/s and with (d)  $\delta = 12$  mm. Note that for clarity in (a) we report the force as a function of midspan position,  $w(L/2, t)$ .

see Fig. S11 [24]). This indicates that the plastically deformed arches manifest nonreciprocity with respect to the loading condition, an observation that it is further supported by the fact that the maximum forces recorded when testing them under *Loading 1* and *Loading 2* are very different (i.e.,  $\max |Q^{(1)}| / \max |Q^{(2)}| \sim 1.75$ ).

While the results reported in Fig. 1 were obtained by indenting the arches at  $\alpha = 15$  mm/s, we want to emphasize that the observed sudden drop in force is a robust feature of the system. To demonstrate this important point, in Figs. 2(a) and 2(c) we focus on the elastically deformed arch and show the evolution of the force when loaded according to *Loading 1* at  $\alpha = 1$  mm/s. Despite the considerably lower speed, the arch still dynamically transitions to an asymmetric configuration, leading to a sudden drop in the recorded force (similar results for the plastically deformed arch are shown in the Supplemental Material, Additional Results [24]). However, the point at which the dynamic transition occurs is affected by the loading rate [see Fig. 2(a)]. By contrast, the drop in force is suppressed as soon as the indenter is offset from the center point [Figs. 2(b) and 2(d)] as in this case the arch deforms asymmetrically from the very beginning [see snapshots in Figs. 2(b) and 2(d)].

$$\bar{x} = \frac{\pi x}{L}, \quad \bar{t} = \frac{\pi^2 t}{L^2} \sqrt{\frac{EI}{A\rho}}, \quad \bar{w}(\bar{x}, \bar{t}) = \frac{w(x, t)}{r}, \quad \bar{w}_i^{(j)}(\bar{x}) = \frac{w_i^{(j)}(x)}{r}, \quad \bar{w}_0(\bar{x}) = \frac{w_0(x)}{r}, \quad \bar{e}^{(j)} = \frac{e^{(j)}}{r}, \quad (2a-f)$$

$$\bar{d}^{(j)}(\bar{t}) = \frac{d^{(j)}(t)}{r}, \quad \bar{p}(\bar{t}) = \frac{L^2 p(t)}{\pi^2 EI}, \quad \bar{Q}^{(j)} = \frac{2Q^{(j)}L^3}{\pi^4 EI r}, \quad \bar{\beta} = \frac{\beta L^2}{\pi^2 \sqrt{\rho AEI}}, \quad \bar{\delta}(\cdot) = \frac{L}{\pi} \delta(\cdot), \quad (2g-k)$$

where  $r = \sqrt{I/A}$  and rewrite Eq. (1) in dimensionless form as

$$\frac{\partial^2 \bar{w}}{\partial \bar{t}^2} + \bar{\beta} \frac{\partial \bar{w}}{\partial \bar{t}} + \left( \frac{\partial^4 \bar{w}}{\partial \bar{x}^4} - \frac{d^4 \bar{w}_0}{d \bar{x}^4} \right) + \bar{p} \frac{\partial^2 \bar{w}}{\partial \bar{x}^2} + \frac{\pi}{2} \bar{Q}^{(j)} \bar{\delta} \left( \bar{x} - \frac{\pi}{2} \right) = 0. \quad (3)$$

For the pinned end conditions considered in this study,

$$\bar{w}(0, \bar{t}) = \bar{w}(\pi, \bar{t}) = 0, \quad \bar{w}''(0, \bar{t}) = \bar{w}''(\pi, \bar{t}) = 0, \quad (4)$$

and, since in our experiment we control the displacement, we impose

$$\bar{w} \left( \frac{\pi}{2}, \bar{t} \right) = \bar{e}^{(j)} + \bar{d}^{(j)}(\bar{t}). \quad (5)$$

It follows that under these conditions the deformed shape  $\bar{w}(\bar{x}, \bar{t})$  can be expressed as a series of sine functions

$$\bar{w}(\bar{x}, \bar{t}) = \bar{w}_0(\bar{x}) + \sum_{n=1}^N a_n(\bar{t}) \sin(n\bar{x}). \quad (6)$$

In the following sections we specialize Eq. (3) to the cases of plastically and elastically deformed shallow arches and obtain the coefficients  $a_n(\bar{t})$  entering in the solution.

### III. NUMERICAL MODEL

Next, to get more insights into the observed nonlinear phenomena, we develop a numerical model. While previous modeling efforts have used quasistatic assumptions to capture the response of shallow arches loaded with an indenter prior to snapping [4,5], the dynamic nature of the transition observed in our tests at  $t = t_{\text{asym}}$  requires a fully dynamic approach. As such, we describe the arches' time-dependent profile  $w(x, t)$  using Kirchhoff plate theory [25] and write the equation of motion for *Loading j* (with  $j = 1, 2$ ) as [4,6,19,26–28]

$$\rho A \frac{\partial^2 w}{\partial t^2} + \beta \frac{\partial w}{\partial t} + EI \left( \frac{\partial^4 w}{\partial x^4} - \frac{d^4 w_0}{dx^4} \right) + p \frac{\partial^2 w}{\partial x^2} + Q^{(j)} \delta \left( x - \frac{L}{2} \right) = 0, \quad (1)$$

where  $A$  and  $I$  are the area and moment of inertia of the cross section, respectively,  $\rho$  and  $E$  are the volumetric density and Young's modulus of the material, respectively, and  $\beta$  represents the viscous damping coefficient. Moreover,  $w_0$  is the initial unstressed position of the midsurface of the arch,  $p$  is the midplane force produced by the stretching of the middle surface, and  $\delta$  is the Dirac delta function.

Next, we introduce the nondimensional variables

#### A. Plastically deformed shallow arch

We start by focusing on plastically deformed shallow arches and note that for these structures the midplane force is [19,20]

$$\bar{p}(\bar{t}) = -\frac{1}{2\pi} \int_0^\pi \left[ \left( \frac{\partial \bar{w}}{\partial \bar{x}} \right)^2 - \left( \frac{d\bar{w}_0}{d\bar{x}} \right)^2 \right] d\bar{x}, \quad (7)$$

and the initial unstressed position of the midsurface is

$$\bar{w}_0 = \bar{e}^{(1)} \sin(\bar{x}), \quad (8)$$

since in all our experiments (i.e., for both *Loading 1* and *Loading 2*) the arches are plastically deformed to be initially curved upwards. Substitution of Eqs. (6), (7), and (8) into Eq. (3), multiplication of all terms by  $\sin(m\bar{x})$  ( $m$  being an integer,  $m = 1, \dots, N$ ) and integration with respect to  $\bar{x}$  from 0 to  $\pi$  yield

$$\ddot{a}_1 + \bar{\beta} \dot{a}_1 + a_1 + \frac{1}{4} \left( 2\bar{e}^{(1)} a_1 + \sum_{k=1}^N k^2 a_k^2 \right) (a_1 + \bar{e}^{(1)}) + q_1^{(j)} = 0 \quad \text{for } n = 1, \quad (9a)$$

$$\ddot{a}_n + \bar{\beta} \dot{a}_n + n^4 a_n + \frac{n^2}{4} \left( 2\bar{e}^{(1)} a_1 + \sum_{k=1}^N k^2 a_k^2 \right) a_n + q_n^{(j)} = 0 \quad \text{for } n = 2, \dots, N, \quad (9b)$$

with

$$q_n^{(j)} = \bar{Q}^{(j)} \sin\left(\frac{n\pi}{2}\right) \quad \text{for } n = 1, \dots, N. \quad (10)$$

Moreover, by substituting Eqs. (6) and (8) into Eq. (5) we obtain

$$-\bar{d}^{(j)} + \bar{e}^{(1)} - \bar{e}^{(j)} + \sum_{j=1}^{\|(N+1)/2\|} -(-1)^j a_{2j-1} = 0. \quad (11)$$

At this point it is important to notice that Eq. (11) describes the behavior of the arch only while it is in contact with the indenter (i.e.,  $|\bar{Q}^{(j)}(t)| > 0$ ). When  $\bar{Q}^{(j)}(t) = 0$  the arch leaves the indenter, Eq. (11) does not hold true anymore, and Eqs. (9) simplify to

$$\ddot{a}_1 + \bar{\beta}\dot{a}_1 + a_1 + \frac{1}{4}\left(2\bar{e}^{(1)}a_1 + \sum_{k=1}^N k^2 a_k^2\right)(a_1 + \bar{e}^{(1)}) = 0 \quad \text{for } n = 1, \quad (12a)$$

$$\ddot{a}_n + \bar{\beta}\dot{a}_n + n^4 a_n + \frac{n^2}{4}\left(2\bar{e}^{(1)}a_1 + \sum_{k=1}^N k^2 a_k^2\right)a_n = 0 \quad \text{for } n = 2, \dots, N. \quad (12b)$$

To obtain the response of the arch upon indentation, we start by numerically solving Eqs. (9) with Runge-Kutta while imposing the constraint given by Eq. (11). We monitor the evolution of  $|\bar{Q}^{(j)}(\bar{t})|$  and when it vanishes immediately switch to Eq. (12), which we numerically solve using the positions and velocities given by Eqs. (9) and Eq. (11) for  $|\bar{Q}^{(j)}(\bar{t})| = 0$  as initial conditions.

Finally, we note that Eqs. (12) also provide the stable inverted equilibrium configuration when solved in the quasistatic limit [i.e.,  $\ddot{a}_n = \dot{a}_n = 0$ ; see the Supplemental Material, Mathematical model for the derivation [24]]. We find that, for plastically deformed arches with  $\bar{e}^{(1)} \geq 4$  the inverted configuration has a smaller rise,

$$\bar{e}^{(2)} = -\frac{1}{2}\left[\bar{e}^{(1)} + \sqrt{(\bar{e}^{(1)})^2 - 16}\right], \quad (13)$$

an observation that supports the nonreciprocal behavior observed in our experiments.

### B. Elastically deformed shallow arch

For an elastically deformed shallow arch (i.e., a postbuckled beam) the midplane force is given by [4,29]

$$\bar{p}(\bar{x}) = \left[ \frac{L^2(L_0 - L)}{L_0\pi^2 r^2} - \frac{1}{2\pi} \int_0^\pi \left( \frac{\partial \bar{w}}{\partial \bar{x}} \right)^2 d\bar{x} \right], \quad (14)$$

and the initial unstressed position of the midsurface is

$$\bar{w}_0 = 0. \quad (15)$$

As for the plastically deformed arch, to obtain the governing equations for  $a_n$  we substitute Eqs. (6), (14), and (15) into Eq. (3), multiply of all terms by  $\sin(m\bar{x})$  ( $m$  being an integer,  $m = 1, \dots, N$ ), and integrate with respect to  $\bar{x}$  from 0 to  $\pi$  to

obtain

$$\ddot{a}_n + \bar{\beta}\dot{a}_n + n^4 a_n - n^2 \left( \Delta\bar{L} - \frac{1}{4} \sum_{k=1}^N k^2 a_k^2 \right) a_n + q_n^{(j)} = 0 \quad \text{for } n = 1, 2, \dots, N, \quad (16)$$

where

$$\Delta\bar{L} = \frac{L^2(L_0 - L)}{L_0\pi^2 r^2}, \quad (17)$$

and  $q_n^{(j)}$  is defined in Eq. (10).

Moreover, by substituting Eqs. (6) and (15) into Eq. (5) we obtain

$$-\bar{d}^{(j)} - \bar{e}^{(j)} + \sum_{j=1}^{\|(N+1)/2\|} -(-1)^j a_{2j-1} = 0. \quad (18)$$

Also for the elastically deformed arch, Eq. (18) describes its behavior only while it is in contact with the indenter (i.e.,  $|\bar{Q}^{(j)}(t)| > 0$ ). When  $\bar{Q}^{(j)}(t) = 0$  the arch leaves the indenter, Eq. (18) does not hold true anymore, and Eq. (16) simplifies to

$$\ddot{a}_n + \bar{\beta}\dot{a}_n + n^4 a_n - n^2 \left( \Delta\bar{L} - \frac{1}{4} \sum_{k=1}^N k^2 a_k^2 \right) a_n = 0, \quad \text{for } n = 1, 2, \dots, N. \quad (19)$$

To obtain the response of the arch upon indentation, we numerically solve Eq. (16), while imposing the constraint given by Eq. (18) when the indenter and the arch are in contact. When  $|\bar{Q}^{(j)}(\bar{t})|$  vanishes, we switch to Eq. (19), which we numerically solve using the positions and velocities given by Eqs. (16) and (18) for  $|\bar{Q}^{(j)}(\bar{t})| = 0$  as initial conditions.

Last, we want to emphasize that Eq. (19) also provides the stable inverted equilibrium configuration when solved in the quasistatic limit (i.e.,  $\ddot{a}_n = \dot{a}_n = 0$ ). As expected, for the elastically deformed arches the two equilibrium configurations are identical.

## IV. NUMERICAL RESULTS

To verify the validity of our numerical model, in Fig. 3(a) we focus on the evolution of the nondimensionalized force,  $|\bar{Q}^{(1)}|$ , and compare the numerical predictions for different values of  $N$  (green and red thin lines) with the experimental results (black line). Since the deformed arch shape observed in experiments [see snapshots in Figs. 1(e) and 1(f) at  $t = 0.26$  s and  $t = 0.19$  s, respectively] cannot be represented with only two modes, for both the plastically and elastically deformed arches the model with  $N = 2$  predicts a nonrealistic large peak force. On the contrary, we find very good agreement between the numerical and experimental results for  $N \geq 3$ , with the model that precisely predicts the sharp drop in the forces at  $\bar{t}_{\text{asym}}$ , the maximum value of the forces and the snapping times  $\bar{t}_{\text{snap}}$  [see Fig. 3(a) and Movie S2 [24]].

Next, we focus on the evolution of the coefficients  $a_n$  and find that [see Fig. 3(b)] (i) the first symmetric mode contributes to the arch deformation during the entire test (i.e.,  $a_1 \neq 0$  for  $\bar{t} > 0$ ); (ii) the antisymmetric mode with amplitude  $a_2$  is suddenly activated at  $\bar{t} = \bar{t}_{\text{asym}}$ , remains almost constant

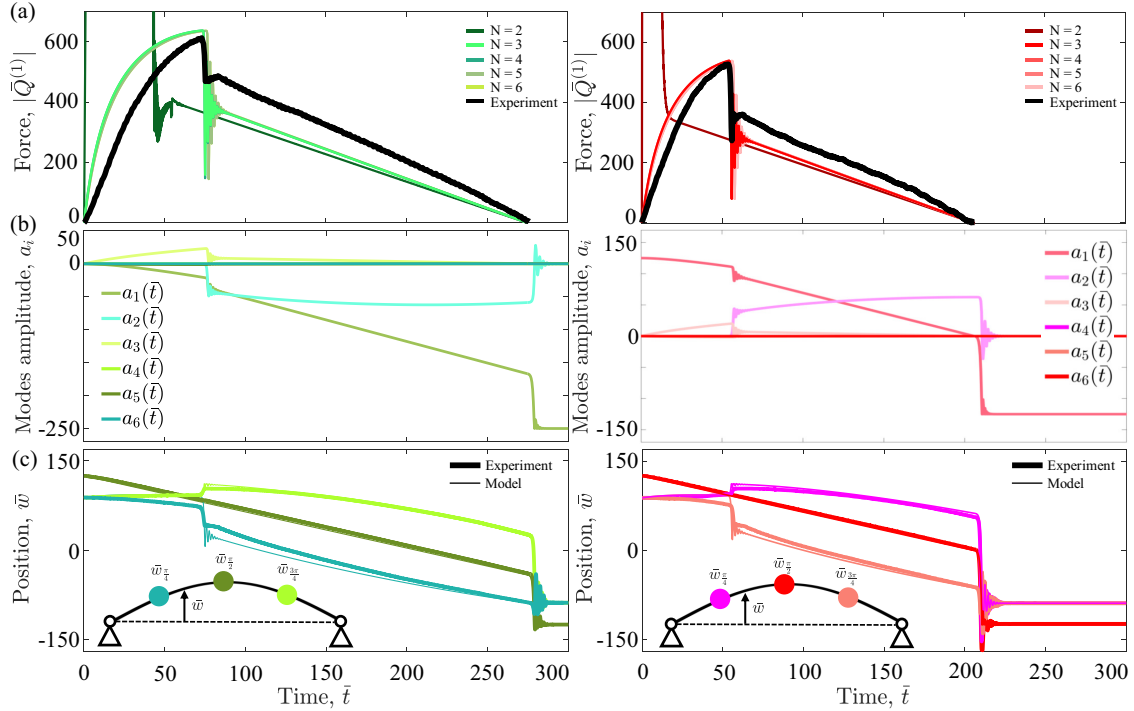


FIG. 3. (a) Comparison between the experimentally measured (black-thick lines) and numerically predicted (green and red thin lines) reaction force  $|\bar{Q}^{(1)}|$  for our plastically (left) and elastically (right) deformed arches subjected to *Loading 1*. (b) Computed mode amplitudes  $a_i$ . (c) Comparison between the experimentally measured (thick lines) and numerically predicted (thin lines) position  $\bar{w}$  for *Loading 1*.

for  $\bar{t}_{\text{asym}} < \bar{t} < \bar{t}_{\text{snap}}$ , and then rapidly vanishes at  $\bar{t} = \bar{t}_{\text{snap}}$ ; (iii)  $a_3$  monotonically increases up to  $\bar{t} = \bar{t}_{\text{asym}}$  and then almost vanishes once the antisymmetric mode is triggered; and (iv)  $a_4(\bar{t})$ ,  $a_5(\bar{t})$ , and  $a_6(\bar{t})$  are very close to zero during the entire test and do not contribute to the overall solution. In full agreement with our experimental observations, such evolution of the modal coefficients results in an asymmetric configuration for  $\bar{t}_{\text{asym}} < \bar{t} < \bar{t}_{\text{snap}}$ , as the displacement  $\bar{w}_{\pi/4}$  and  $\bar{w}_{3\pi/4}$  predicted by the model deviate from each other [see Fig. 3(c)].

Having confirmed the ability of our dynamical model to accurately capture the response of the arches for  $N \geq 3$ , we next use it with  $N = 3$  to explore the effect of the initial nondimensional rise  $\bar{e}^{(1)}$  (with  $\bar{e}^{(1)} < 142$ , since for larger rises the Kirchhoff plate theory is not accurate anymore [25]). As expected, we find that both the maximum force,  $\max |\bar{Q}^{(j)}|$ , and the snapping time,  $\bar{t}_{\text{snap}}^{(j)}$ , monotonically decrease with  $\bar{e}^{(1)}$  [see Figs. 4(a)–4(c)]. Similarly, also the drop in force at  $\bar{t} = \bar{t}_{\text{asym}}$ ,  $\Delta \bar{Q}^{(j)}$  [see Fig. 3(d)] monotonically decreases and eventually vanishes for  $\bar{e}^{(1)} \leq 9.6$  for the elastically deformed arches and for  $\bar{e}^{(1)} \leq 11.9$  and  $\bar{e}^{(1)} \leq 6.2$  for the plastically deformed ones when tested according to *Loading 1* and *Loading 2*, respectively. While all arches for which  $\Delta \bar{Q}^{(j)} > 0$  manifest a sudden activation of the antisymmetric mode prior to snapping, those with  $\Delta \bar{Q}^{(j)} = 0$  do not exhibit such additional dynamic transition from the symmetric to the asymmetric shape. Further, we find that the nonreciprocity in the response of the plastically deformed shallow arches is a robust feature, as for a wide range of  $\bar{e}^{(1)}$ ,  $\bar{t}_{\text{snap}}^{(1)} > \bar{t}_{\text{snap}}^{(2)}$ . To better characterize such nonreciprocity, in Fig. 4(e) we report evolution of the difference between the snapping times for *Loading 1* and 2,

$\Delta \bar{T} = \bar{t}_{\text{snap}}^{(1)} - \bar{t}_{\text{snap}}^{(2)}$ , as a function of  $\bar{e}^{(1)}$ . We find that  $\Delta \bar{T}$  linearly decreases as  $\bar{e}^{(1)}$  is reduced and eventually vanishes when  $\bar{e}^{(1)} = 4$ .

Next, we use our dynamical model to investigate the effect of the loading rate  $\alpha$  on the mechanical response of the system. Towards this end, we consider an elastically deformed arch with  $\bar{e}^{(1)} \sim 125$  and simulate its behavior when indented with  $\alpha \in [0.01, 15]$  mm/s (note that in all our analyses  $\beta = 0.8$ ). Two key features emerge from the results shown in Fig. 5. First, all the curves are identical for  $w(L/2, t) > 9.58$  mm, indicating that the initial response of the arches is fully determined by the instantaneous arch position and not affected by  $\alpha$ . Second,  $\alpha$  has a strong effect on the location of the asymmetric transition and magnitude of the corresponding jump in force. Specifically, three distinct regions can be identified: (i) for  $0.13$  mm/s  $< \alpha \leq 15$  mm/s the force at which the asymmetric transition occurs and the magnitude of the jump monotonically decreases as the indentation speed becomes smaller (i.e., the drop in force happens for larger values of  $w(L/2, t)$ ); (ii) for  $0.01$  mm/s  $< \alpha \leq 0.13$  mm/s the transition is triggered at significantly smaller values of  $w(L/2, t)$  (and these decrease as  $\alpha$  decreases). This is because with simply supported boundary conditions the activation of the antisymmetric mode is always accompanied by a sudden drop in the force (differently from clamp-clamp boundary conditions [see Fig. S7 [24]]) and such a drop cannot be achieved for  $w(L/2, t) > 9.58$  mm; and (iii) for  $\alpha \leq 0.01$  mm/s the arch does not exhibit a dynamic transition (i.e., the jump in force vanishes). It maintains a symmetric profile during the entire test and approaches the curve obtained when solving Eq. (16) in the quasistatic limit (i.e., with  $\ddot{a}_n = \dot{a}_n = 0$ ; see

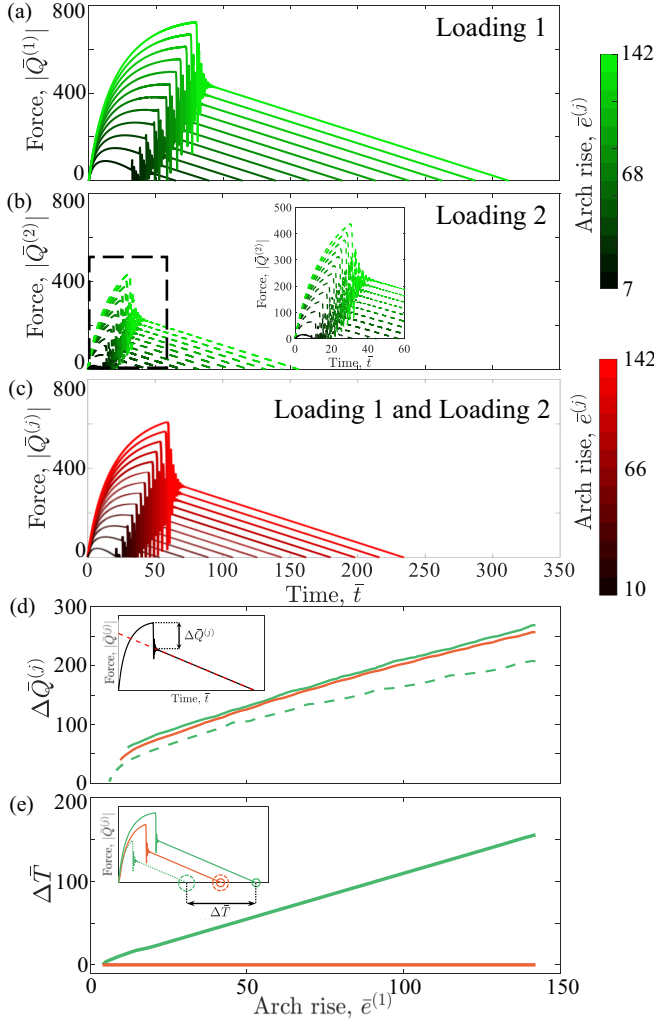


FIG. 4. (a)–(c) Numerically predicted evolution of  $\bar{Q}^{(j)}$  for different values of rise when indenting at  $\alpha = 15$  mm/s. Parametric study by varying  $\bar{e}^{(j)}$ : plastic shallow arch under (a) *Loading 1* and (b) *Loading 2*, (c) elastic shallow arch; (d) sudden force drop amplitude  $\Delta\bar{Q}^{(j)}$  and (e) difference in the snapping time  $\Delta\bar{T} = \bar{t}_{\text{snap}}^{(1)} - \bar{t}_{\text{snap}}^{(2)}$ .

Fig. 5, empty-circle markers and Fig. S10 in Supplemental Material, Additional Results [24].

Finally, we focus on shallow arches with  $\bar{e}_1 \leq 9$ . As shown in Fig. 6, for all these structures the force is smooth [Figs. 6(a) and 6(b)] and the symmetric shape is maintained during the entire test, i.e.,  $a_2 = 0$  [see Figs. 6(c) and 6(d)]. However, we also find a significant difference between the elastically and plastically deformed arches. While the former snap for any  $\bar{e}^{(1)} > 0$ , for the latter snapping occurs only for  $\bar{e}^{(1)} > 4$  when the force  $\bar{Q}^{(1)}$  still crosses zero [see Fig. 6(a)]. Note that such feature is also predicted by Eq. (13), as  $\bar{e}_2$  is not a real number for  $\bar{e}_1 < 4$  anymore, and, therefore, the inverted equilibrium configuration does not exist anymore. As such, when a plastically deformed arch with  $\bar{e}_1 = 4$  is forced to the inverted equilibrium configuration  $\bar{e}^{(2)}$ , it immediately returns to the initial shape once the indenter is removed [see Fig. 6(e)], further evidence of the lack of bistability. Thus,

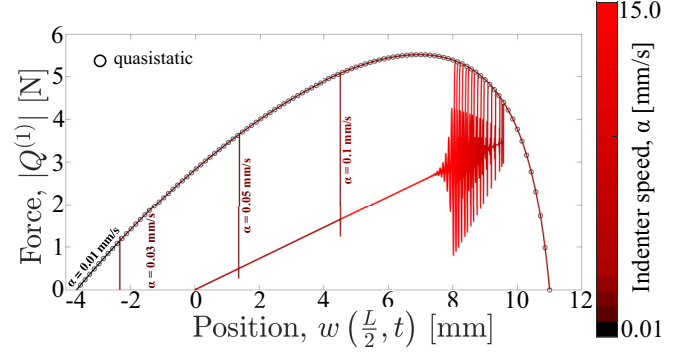


FIG. 5. Numerically predicted evolution of  $|\bar{Q}^{(1)}|$  for different indentation rates  $\alpha \in [0.01, 15]$  mm/sec. In these analyses we consider an elastically deformed shallow arch with rise  $\bar{e}^{(1)} \sim 125$ . The circular markers corresponds to the quasistatic solution.

$\bar{e}^{(1)} = 4$  represents a critical snapping threshold for the plastically deformed shallow arches when transversely loaded. Differently, elastically deformed arches always maintain the stable inverted equilibrium configuration [see Fig. 6(f)].

## V. CONCLUSIONS

To summarize, we have experimentally investigated the nonlinear response of hinged shallow arches subjected to midpoint displacement and found a surprisingly rich dynamic behavior. Further, we have developed a fully dynamic model that can accurately predict the response observed in the experiments and, therefore, can be used as a powerful tool for the *a priori* design and optimization of such nonlinear mechanical systems. Given all the interesting features exhibited by hinged shallow arches subjected to a midpoint

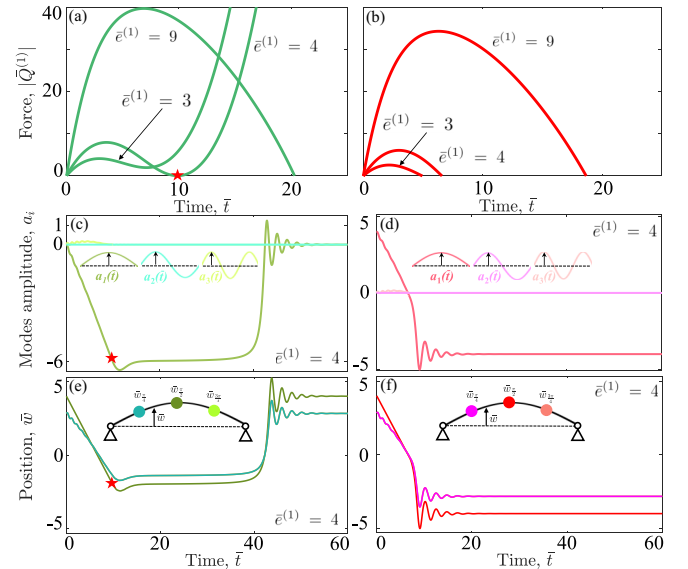


FIG. 6. Arches with low rises  $\bar{e}^{(1)} \leq 9$ : computed quasistatic reaction forces  $|\bar{Q}^{(1)}|$  of (a) plastic and (b) elastic shallow arches for *Loading 1* with corresponding modes amplitudes  $a_i$  (c), (d) and positions  $\bar{w}$  (e), (f). The red star represents when the inverted equilibrium condition  $\bar{e}_2$  is reached by the indenter.

displacement (including nonreciprocity, sudden strength loss, and critical threshold for snapping), we envision these structural elements could serve as building blocks for the next generation of nonlinear mechanical metamaterials designed to manipulate the propagation of elastic pulses in unprecedented ways.

#### ACKNOWLEDGMENTS

K.B. acknowledges support from the National Science Foundation under Grant No. DMR-1420570 and from the Army Research Office under Grant No. W911NF-17-1-0147.

- 
- [1] M. Trachtenberg and I. Hyman, *Architecture, from Prehistory to Post-modernism: The Western Tradition* (H. N. Abrams, New York, 1986).
- [2] J. E. Gordon, *Structures: Or Why Things Don't Fall Down* (Da Capo Press, New York, 2009).
- [3] N. Hu and R. Burgueño, *Smart Mater. Struct.* **24**, 063001 (2015).
- [4] A. Pandey, D. E. Moulton, D. Vella, and D. P. Holmes, *Europhys. Lett.* **105**, 24001 (2014).
- [5] P. Harvey Jr. and L. Virgin, *Int. J. Solids Struct.* **54**, 1 (2015).
- [6] M. Gomez, D. E. Moulton, and D. Vella, *Nat. Phys.* **13**, 142 (2017).
- [7] R. M. Neville, R. M. J. Groh, A. Pirrera, and M. Schenk, *Phys. Rev. Lett.* **120**, 254101 (2018).
- [8] J. M. T. Thompson, *Int. J. Bifurcation Chaos* **27**, 1730029 (2017).
- [9] M. E. Pontecorvo, S. Barbarino, G. J. Murray, and F. S. Gandhi, *J. Intell. Mater. Syst. Struct.* **24**, 274 (2013).
- [10] C. Hsu and W. Hsu, *J. Micromech. Microeng.* **13**, 955 (2003).
- [11] K. Das and R. Batra, *Smart Mater. Struct.* **18**, 115008 (2009).
- [12] M. Gomez, D. E. Moulton, and D. Vella, *Phys. Rev. Lett.* **119**, 144502 (2017).
- [13] S. Shan, S. H. Kang, J. R. Raney, P. Wang, L. Fang, F. Candido, J. A. Lewis, and K. Bertoldi, *Adv. Mater.* **27**, 4296 (2015).
- [14] J. S. Han, J. S. Ko, and J. G. Korvink, *J. Micromech. Microeng.* **14**, 1585 (2004).
- [15] M. R. Shankar, M. L. Smith, V. P. Tondiglia, K. M. Lee, M. E. McConney, D. H. Wang, L.-S. Tan, and T. J. White, *Proc. Natl. Acad. Sci. USA* **110**, 18792 (2013).
- [16] N. Nadkarni, A. F. Arrieta, C. Chong, D. M. Kochmann, and C. Daraio, *Phys. Rev. Lett.* **116**, 244501 (2016).
- [17] J. R. Raney, N. Nadkarni, C. Daraio, D. M. Kochmann, J. A. Lewis, and K. Bertoldi, *Proc. Natl. Acad. Sci. USA* **113**, 9722 (2016).
- [18] S. P. Timoshenko and J. M. Gere, *Theory of Elastic Stability* (Courier Corporation, Indianapolis, 2009).
- [19] M. H. Lock, *AIAA J.* **4**, 1249 (1966).
- [20] J. S. Humphreys, *AIAA J.* **4**, 878 (1966).
- [21] G. Simitses and D. H. Hodges, *Fundamentals of Structural Stability* (Butterworth-Heinemann, London, 2006).
- [22] A. B. Pippard, *Eur. J. Phys.* **11**, 359 (1990).
- [23] P. Patrício, M. Adda-Bedia, and M. B. Amar, *Physica D* **124**, 285 (1998).
- [24] See Supplemental Material at <http://link.aps.org/supplemental/10.1103/PhysRevE.101.053004> for a description of fabrication and experiments, details on the model, and supporting movies, which includes Refs. [4,6,19,20,25–29].
- [25] G. Kirchhoff, *J. reine angew. Math.* **40**, 51 (1850).
- [26] Y. Fung and A. Kaplan, U.S. National Advisory Committee for Aeronautics Technical Note No. 2840, November (1952).
- [27] A. Nayfeh and D. Mook, *Nonlinear Oscillations* (Wiley, New York, 1979).
- [28] J.-S. Chen, W.-C. Ro, and J.-S. Lin, *Int. J. Non-Linear Mech.* **44**, 66 (2009).
- [29] J.-S. Chen and S.-Y. Hung, *Appl. Math. Model.* **36**, 1776 (2012).

# Supporting Information for *Snapping of hinged arches under displacement control: strength loss and non-reciprocity*

## **S1 Fabrication**

The arches considered in this study comprise of a metallic beam and two rotating hinges. All beams have a width  $b = 10$  mm, a length  $l = 104.5$  mm and are made of spring steel shims (McMaster-Carr product ID: 9014K611) with thickness  $h = 0.3048$  mm and Young's modulus  $E = 170$  GPa, while all hinges are realized using Lego components. Specifically, as shown in Fig. S1, the hinges comprise the following components: (i) a round brick  $2 \times 2$  with axle hole (LEGO part 4249139); (ii) an axle (LEGO part 3705); (iii) axle and pin connectors angled at 180 degrees (LEGO part 32034). Note that in order to ensure a tight connection between the beam and the hinges, slits of 3 mm length and 0.33 mm width are cut into both arms using a vertical knee drilling milling machine with slitting saw (Vectrax); (iv) two bushes (LEGO part 32123); and (v) a round brick  $4 \times 4$  with a center axle hole (LEGO part 4211097). In our setup we use two of these hinges with their  $4 \times 4$  round brick connected and glued (using Krazy Glue *All purposes*) to a Lego plate (LEGO part 91405) with their axels at a distance  $L = 120$  mm from each other.

In the remaining part of this Section we first describe how we fabricate our *plastically deformed* shallow arches and then report our manufacturing process for the *elastically deformed* ones.

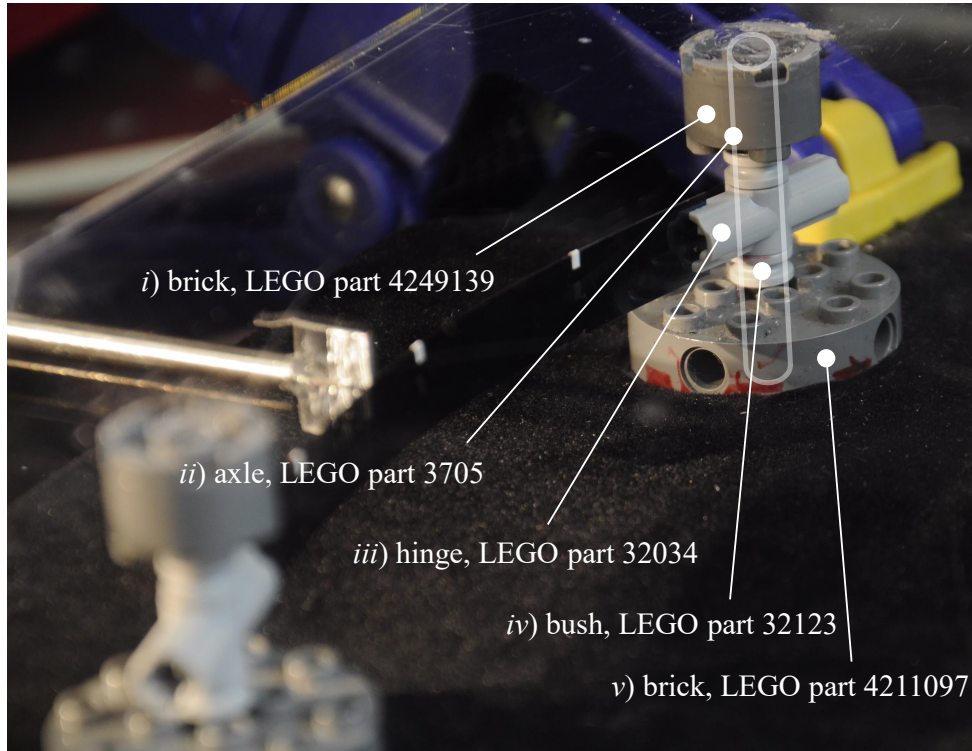


Figure S1: Picture of the hinge used to build our arches. The parts used to fabricate them are highlighted.

### S1.1 Plastically deformed arches

As shown in Fig. S2, our plastically deformed arches are fabricated using the following 5 steps:

**Step 1:** a strip of length  $l$  (with  $l \in [104.0, 104.7]$  mm) and width  $b = 10$  mm is cut with a shearing tool out of the steel shim. The strip is visually inspected to make sure it does not have any residual bending induced by the cutting procedure.

**Step 2:** Iron cylinders of diameter 34 and 25 mm are used to plastically deform the steel beam into a sinusoidal-like shape.

**Step 3:** The shape of the plastically deformed arch is visually compared with that of the target sinusoidal profile (which is laser cut out of an acrylic sheet with thickness 12.7 mm) to make sure the obtained shape is close enough to the desired one. In the unlikely event the arch has a very different shape with respect the benchmark, we either repeat Step 2 or start over from Step

1.

**Step 4:** Both ends of the plastically deformed arch are inserted into the cuts of the LEGO connectors and glue (*Krazy Glue All purposes*) is applied to prevent any sliding.

**Step 5:** The plastically deformed arch (with end-to-end distance  $L = 120$  mm) is connected to the LEGO supports (which are separated by a distance  $L = 120$  mm). Specifically, the two axles (LEGO part 3705) are slid into the two hinges connected to the arch (LEGO part 32034) and two LEGO bushes (LEGO part 32123) are added on the axles to prevent other movements rather than rotation of the hinges. Lastly, an acrylic plate with two LEGO round bricks (LEGO part 4249139) glued on it is fixed on the top to prevent bending of the axles. The arch is now ready to be tested.

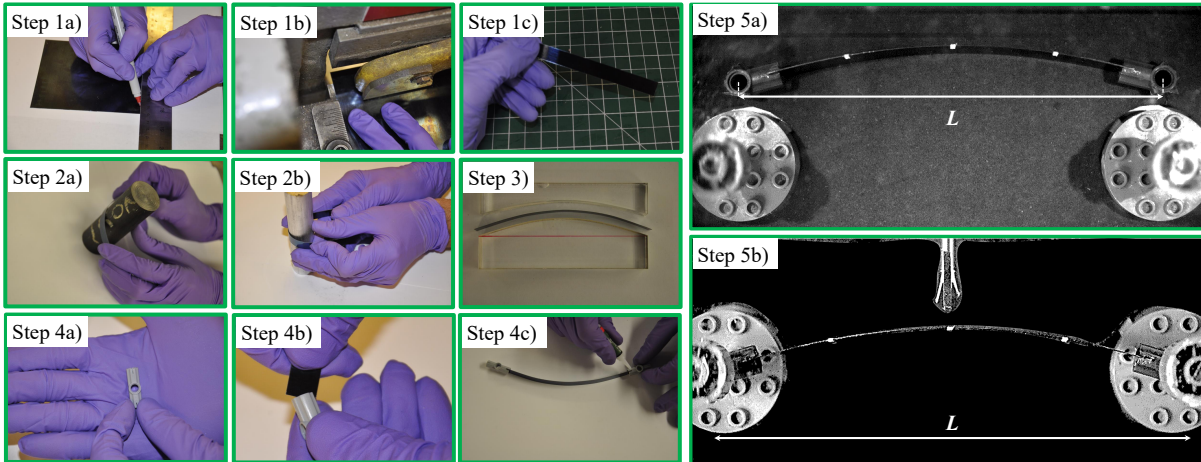


Figure S2: Fabrication steps to manufacture a plastically deformed shallow arch.

## S1.2 Elastically deformed arches

As shown in Fig. S3, our elastically deformed arches are fabricated using the following 3 steps:

**Step 1:** as for the plastically deformed arches, a strip of length  $l$  (with  $l \in [104.0, 104.7]$  mm) and width  $b = 10$  mm is cut out of the steel shim by using a shearing tool. The strip is visually

inspected to make sure it does not have any residual bending induced by the cutting procedure.

**Step 2:** Both ends of the steel are inserted into the cuts of the Lego connectors and glue (Krazy Glue *All purposes*) is applied to prevent any sliding.

**Step 3:** an axial force is manually applied to the specimen (steel strip + LEGO connectors) of total length  $L_0 > L$  mm to buckle it and form an arch with end-to-end distance  $L = 120$  mm. Specifically, the two axles (LEGO part 3705) are slid into the two hinges connected to the arch (LEGO part 32034) and two LEGO bushes (LEGO part 32123) are added on the axles to prevent other movements rather than rotation of the hinges. Lastly, an acrylic plate with two LEGO round bricks (LEGO part 4249139) glued on it is fixed on the top to prevent bending of the axles. The arch is now ready to be tested.

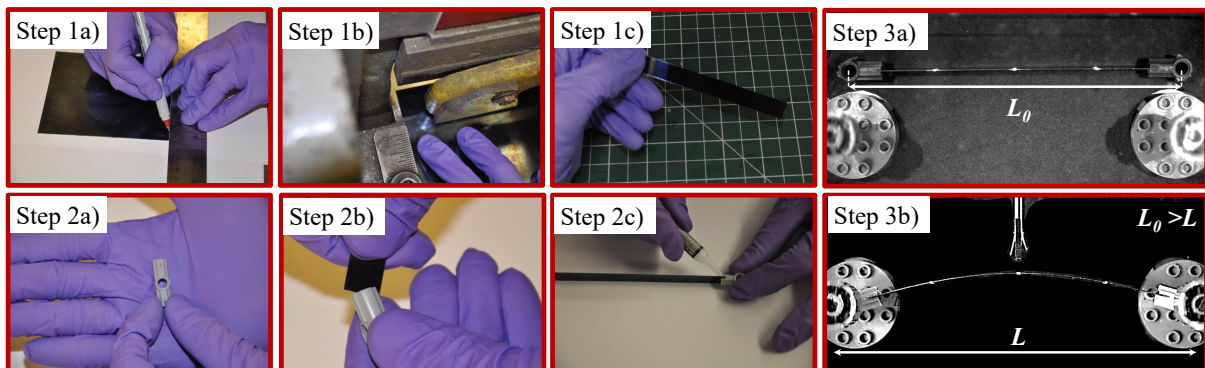


Figure S3: Fabrication steps to manufacture an elastically deformed shallow arch

## S2 Testing

In all our tests we used an indenter (see inset in Fig. S4) to push the central part of the arches at a constant velocity of 15 mm/s (via a motorized translation stage - LTS300, Thorlabs). During our tests the reaction force is measured using a 10 lb load cell (LSB200 Miniature S-Beam Jr. Load cell, FUTEK Advanced Sensor Technology, Inc.). Moreover, a high speed camera (Photron Mini Series) is mounted above the testing area (white dashed line) to track the displacements of three markers positioned at  $L/4$ ,  $L/2$  and  $3L/4$ . The camera records the entire experiment from the contact between the arch and the indenter up to the snapping at a rate of 6400 fps.

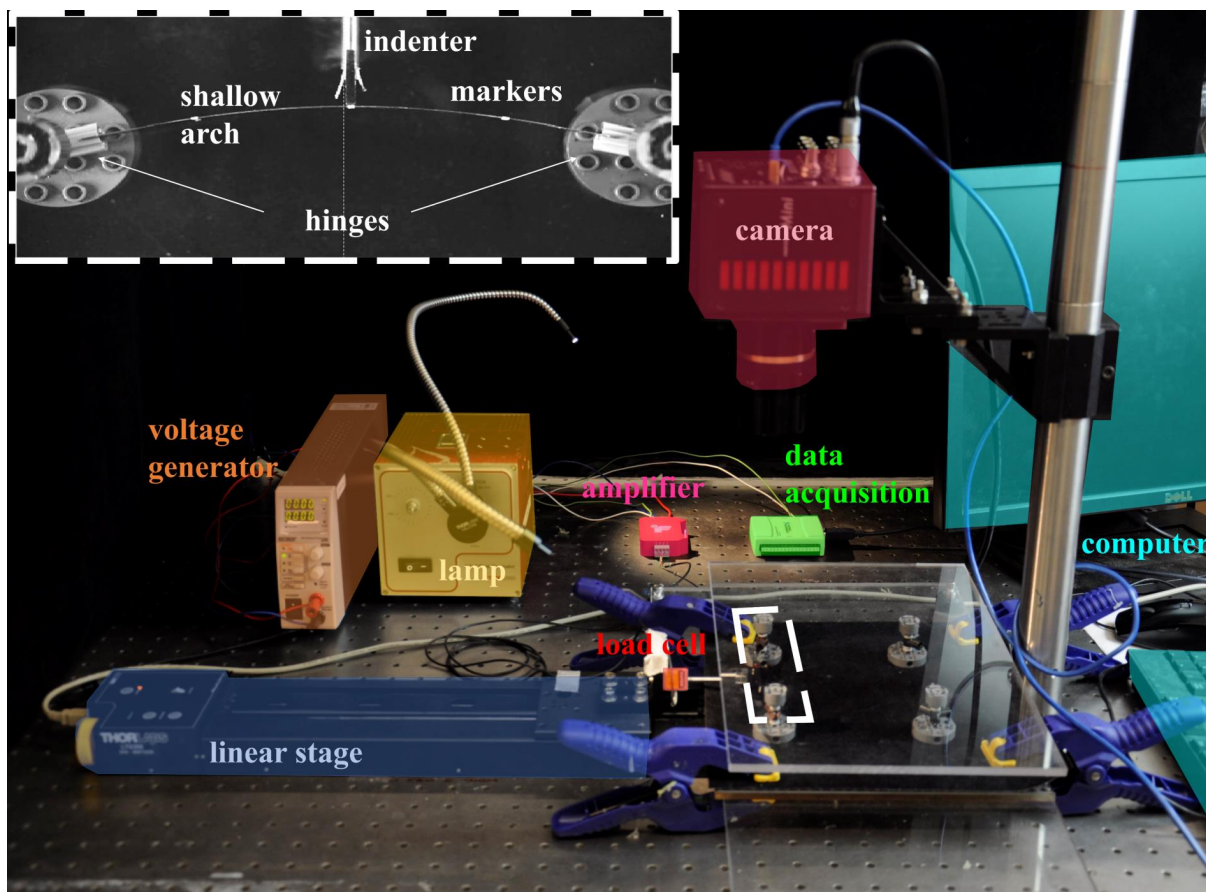


Figure S4: Experimental setup. Components of the experimental setup used to test our arches.

### S3 Mathematical model

To get a better understanding of the dynamic response of our shallow arches, we investigate their behavior analytically. Towards this end, we consider a shallow arch of span  $L$ , thickness  $h$  and initial sinusoidal shape. The arch is pinned at both ends and a monotonically increasing displacement is applied to its midpoint, causing the time-dependent transverse profile  $w(x, t)$  (which is defined positive for positive values of  $z$ ). As shown in Fig. S5 we consider two loading cases:

- *Loading 1* in which the arch is initially curved upwards, so that its shape is described by

$$w_i^{(1)} = e^{(1)} \sin\left(\frac{\pi x}{L}\right) \quad \text{with } e^{(1)} > 0,$$

and the applied displacement,  $d^{(1)} < 0$ , pushes it downwards (see Fig. S5 - top);

- *Loading 2* in which the arch is initially curved downwards, so that its shape is described by

$$w_i^{(2)} = e^{(2)} \sin\left(\frac{\pi x}{L}\right) \quad \text{with } e^{(2)} < 0,$$

and the applied displacement,  $d^{(2)} > 0$  pushes it upwards (see Fig. S5- bottom).

In all our analyses we use  $\rho = 7850 \text{ kg/m}^3$ ,  $A = 3.05 \text{ mm}^2$ ,  $E = 170 \text{ GPa}$ ,  $I = 0.02 \text{ mm}^4$  (all values that are measured) and  $\beta = 0.8$  (value that is chosen to better capture the response observed in our tests). Moreover, to capture the effect of unavoidable imperfections introduced either during testing or fabrication in all our analyses we introduce to the initial profile  $w_i^{(j)}$  a small initial antisymmetric geometric imperfection  $ra_2(0) \sin(2\pi x/L)$  with  $a_2(0) = 10^{-34}\bar{e}^{(1)}$  for *Loading 1* and  $a_2(0) = 10^{-10}\bar{e}^{(1)}$  for *Loading 2* of the plastically deformed arches, while  $a_2(0) = 10^{-26}\bar{e}^{(1)}$  is introduced for both *Loading 1* and *Loading 2* for the elastically deformed arch.

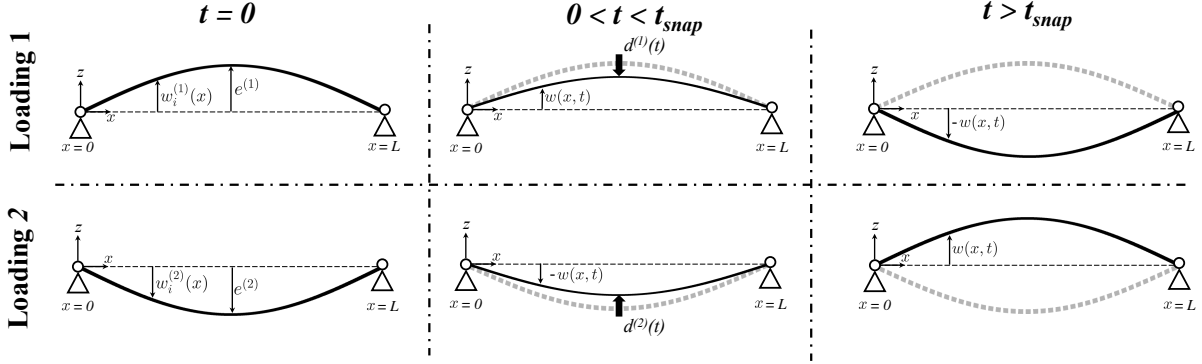


Figure S5: The two loading conditions (*Loading 1* top of the Figure, *Loading 2* bottom of the Figure) for the plastically deformed and elastically deformed shallow arches.

We want to emphasize that for the plastically deformed arch  $\bar{w}_0 \neq 0$  (where  $\bar{w}_0 = w_0/r$  denotes the nondimensional initial unstressed configuration) and the dynamical response of the system to *Loading 1* and *Loading 2* is very different. Such non-reciprocity is clearly revealed by Eq. (11), which takes two distinct forms for *Loading 1* and *Loading 2*

$$-\bar{d}^{(1)} + \sum_{j=1}^{\|(N+1)/2\|} -(-1)^j a_{2j-1} = 0 \quad \text{for } \textit{Loading 1} \quad (\text{S3a})$$

$$-\bar{d}^{(2)} + \bar{e}^{(1)} - \bar{e}^{(2)} + \sum_{j=1}^{\|(N+1)/2\|} -(-1)^j a_{2j-1} = 0 \quad \text{for } \textit{Loading 2} \quad (\text{S3b})$$

Further, for a plastically deformed arch the two stable equilibrium configurations are different (i.e.  $\bar{w}_i^{(1)}(\bar{x}) \neq \bar{w}_i^{(2)}(\bar{x})$ ) - another indication of non-reciprocal behavior. While  $\bar{w}_i^{(1)}(\bar{x})$  is determined during fabrication, the stable inverted equilibrium condition  $\bar{w}_i^{(2)}(\bar{x})$  can be obtained by solving Eqs. (12) in the quasi-static limit. Specifically, for  $\ddot{a}_n = \dot{a}_n = 0$  ( $n = 1, 2, \dots, N$ ), Eqs. (12) reduces to a non-linear system of equation in  $a_n$  ( $n = 1, 2, \dots, N$ ) that admits the solution

$$a_1 = -\frac{1}{2} \left( 3\bar{e}^{(1)} + \sqrt{(\bar{e}^{(1)})^2 - 16} \right), \quad (\text{S4a})$$

$$a_n = 0, \quad n = 2, \dots, N \quad (\text{S4b})$$

Finally, by substituting Eqs. (S4) into Eq. (6) the static inverted equilibrium condition is obtained as

$$\bar{w}_i^{(2)}(\bar{x}) = \bar{w}_0(\bar{x}) - \frac{1}{2} \left( 3\bar{e}^{(1)} + \sqrt{(\bar{e}^{(1)})^2 - 16} \right) \sin(\bar{x}) = -\frac{1}{2} \left( \bar{e}^{(1)} + \sqrt{(\bar{e}^{(1)})^2 - 16} \right) \sin(\bar{x}), \quad (\text{S5})$$

from which we get

$$\bar{e}^{(2)} = -\frac{1}{2} \left( \bar{e}^{(1)} + \sqrt{(\bar{e}^{(1)})^2 - 16} \right). \quad (\text{S6})$$

Note that Eqs. (S4), (S5) and (S6) hold true only for  $\bar{e}^{(1)} \geq 4$ . For  $\bar{e}^{(1)} \leq 4$  the plastically deformed shallow arch loses its bistability and, therefore, does not have a static inverted equilibrium configuration.

By contrast, for an elastically deformed shallow arch  $\bar{w}_0 = 0$  and the dynamical response of the system to *Loading 1* and *Loading 2* is identical. Such reciprocity is clearly revealed by Eq. (18) which takes the same forms for *Loading 1* and *Loading 2*

$$-\bar{d}^{(1)} - \bar{e}^{(1)} + \sum_{j=1}^{\|(N+1)/2\|} -(-1)^j a_{2j-1} = 0 \quad \text{for } \textit{Loading 1} \quad (\text{S7a})$$

$$-\bar{d}^{(2)} - \bar{e}^{(2)} + \sum_{j=1}^{\|(N+1)/2\|} -(-1)^j a_{2j-1} = 0 \quad \text{for } \textit{Loading 2} \quad (\text{S7b})$$

Further, for an elastically deformed shallow arch  $\bar{w}_i^{(2)}(\bar{x}) = -\bar{w}_i^{(1)}(\bar{x})$  and  $\bar{e}^{(2)} = -\bar{e}^{(1)}$ .

## S4 Additional results

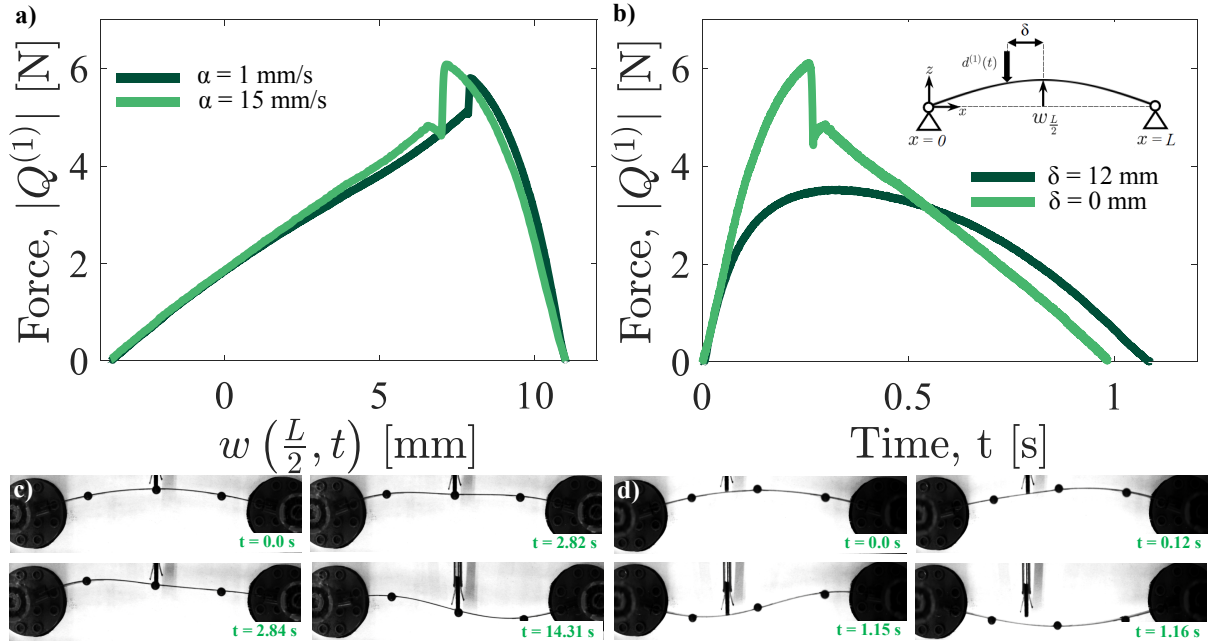


Figure S6: (a)-(b) Forces recorded when indenting a plastically deformed arch according to *Loading 1* (a) at  $\alpha = 1$  mm/s and 15 mm/s and (b) with  $\delta = 0$  and 12 mm. (c)-(d) Snapshots of our plastically deformed arch when tested at (c)  $\alpha = 15$  mm/s and with (d)  $\delta = 12$  mm. Note that for clarity in (a) we report the force as a function of mid-span position,  $w(L/2, t)$ .

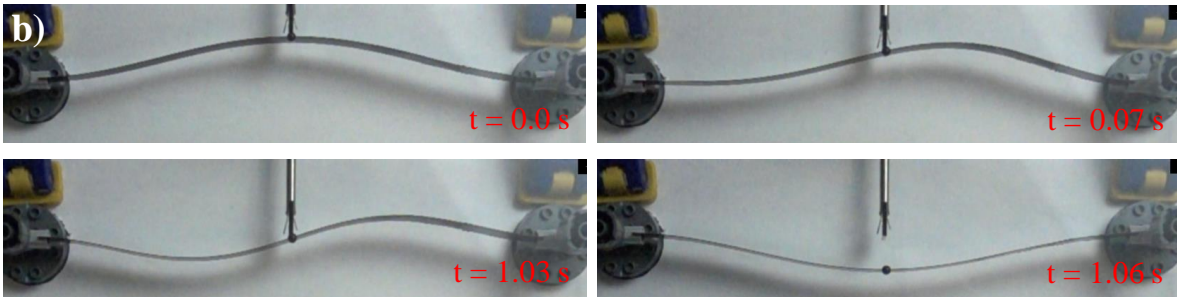
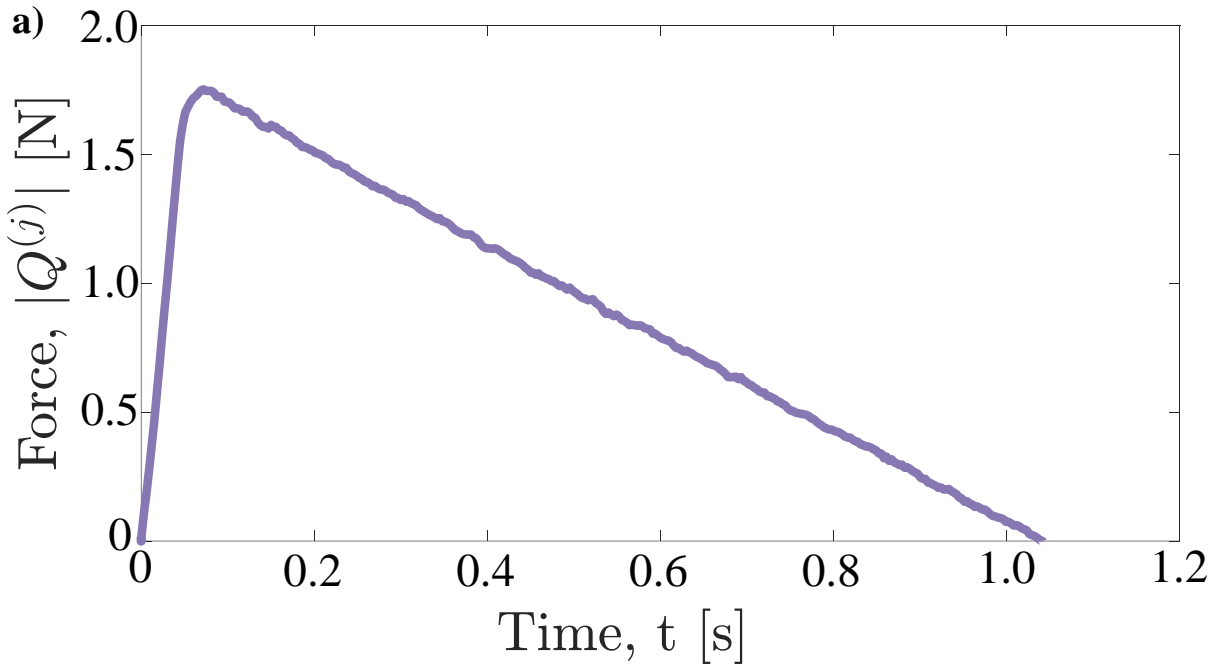


Figure S7: Force recorded when indenting an elastically deformed clamped arch at  $\alpha = 15$  mm/s (with no offset in loading). Note that both ends of the arch are clamped. (b) Snapshots of our elastically deformed arch when tested with  $\alpha = 15$  mm/s and  $\delta = 0$  mm.

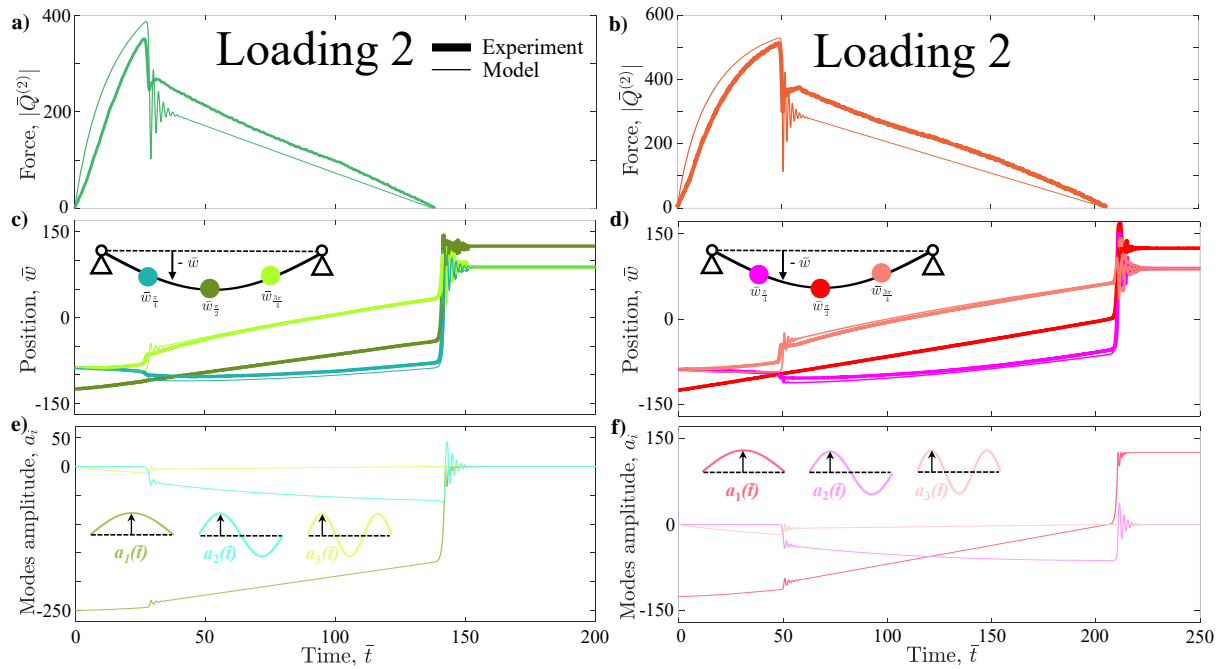


Figure S8: Comparison between numerical (thin lines) and experimental (thick lines) for the plastically (left column) and elastically (right column) deformed shallow arch subjected to *Loading 2*. (a)-(b) Evolution of the nondimensional force,  $\bar{Q}^{(2)}$ , as a function of the nondimensional time,  $\bar{t}$ . (c)-(d) Evolution of the position at  $\bar{x} = \pi/4$ ,  $\bar{w}_{\pi/4}$ , at  $\bar{x} = \pi/2$ ,  $\bar{w}_{\pi/2}$ , and at  $\bar{x} = 3\pi/4$ ,  $\bar{w}_{3\pi/4}$ , as a function of the nondimensional time,  $\bar{t}$ . (e)-(f) Evolution of the modal amplitudes,  $a_i$  (with  $i = 1, 2, 3$ ) as a function of the nondimensional time,  $\bar{t}$ . Note that in this case only numerical predictions are reported.

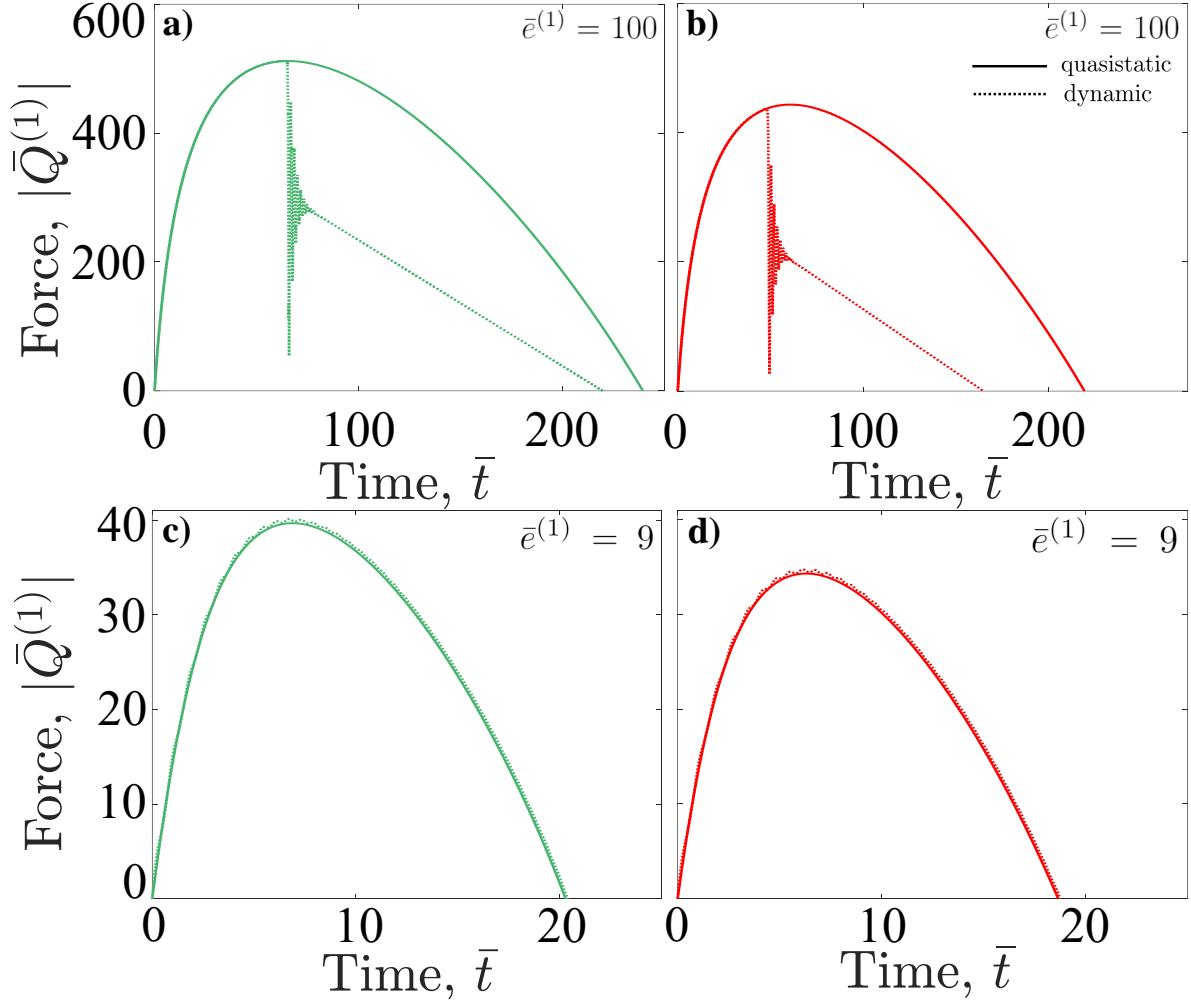


Figure S9: Comparison between the reaction force,  $|\bar{Q}^{(1)}|$ , computed using the full dynamic model (dashed line) and a quasi-static version of the model (solid line). The full dynamic results are obtained by solving either Eq. (9) (for the plastically deformed arch) or Eq. (16) (for the elastically deformed arch). The quasistatic results are obtained by solving either Eq. (9) (for the plastically deformed arch) or Eq. (16) (for the elastically deformed arch) with  $\ddot{a}_n = \dot{a}_n = 0$  ( $n = 1, 2, 3$ ). In this case Eq. (9) and Eq. (16) reduce to a non-linear system of equations in  $a_n$  (with  $n = 1, \dots, N$ ) and  $\bar{Q}^{(j)}$  which is solved using the MATLAB routine *fsolve* (see attached MATLAB codes). (a)-(b) We find that for large rises (such as  $\bar{e}_1 = 100$ ) the quasi-static model does not capture the sudden drop in force, which is instead accurately predicted by the dynamic model. (c)-(d) We find that for arches with low rises ( $\bar{e}_1 = 9$  for which the sudden drop in the force does not occur) the reaction force computed using the quasi-static model is almost identical to the one obtained using the fully dynamic model. All these forces are obtained for *Loading 1*. Green lines correspond to plastically deformed arches, while red lines correspond to elastically deformed ones

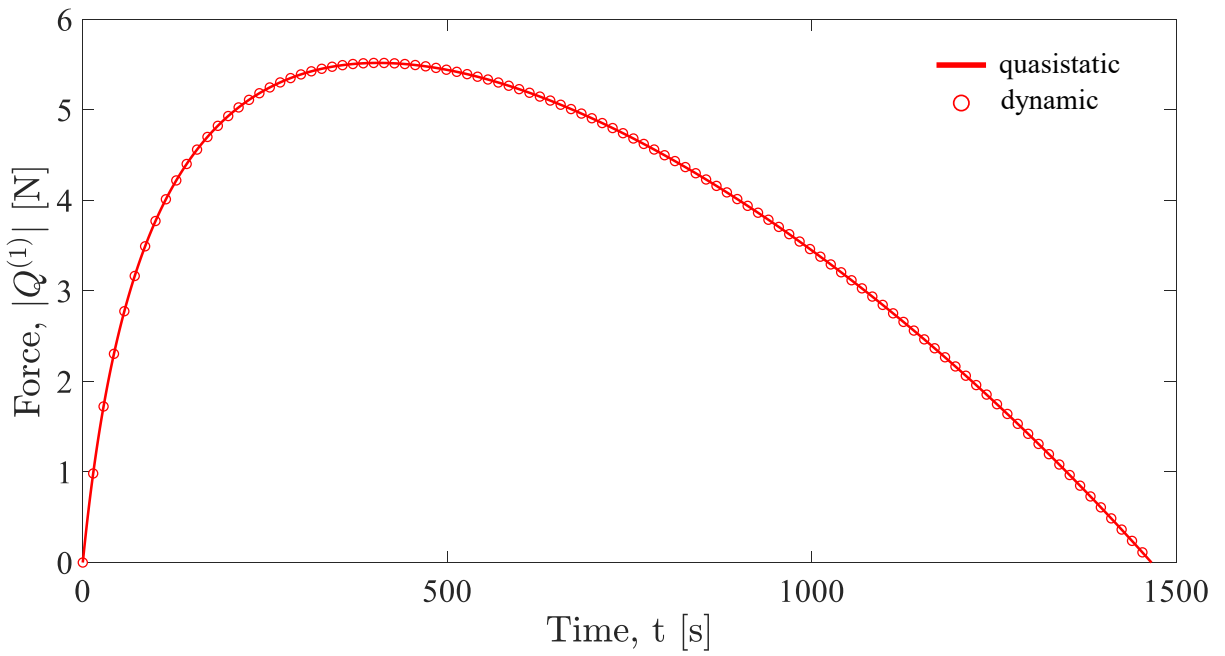


Figure S10: Comparison between the reaction forces,  $|Q^{(1)}|$ , for the elastically deformed arch computed using the full dynamic model (empty circles) and a quasi-static version of the model (solid line) both for an indenter speed  $\alpha = 0.01\text{mm/sec}$

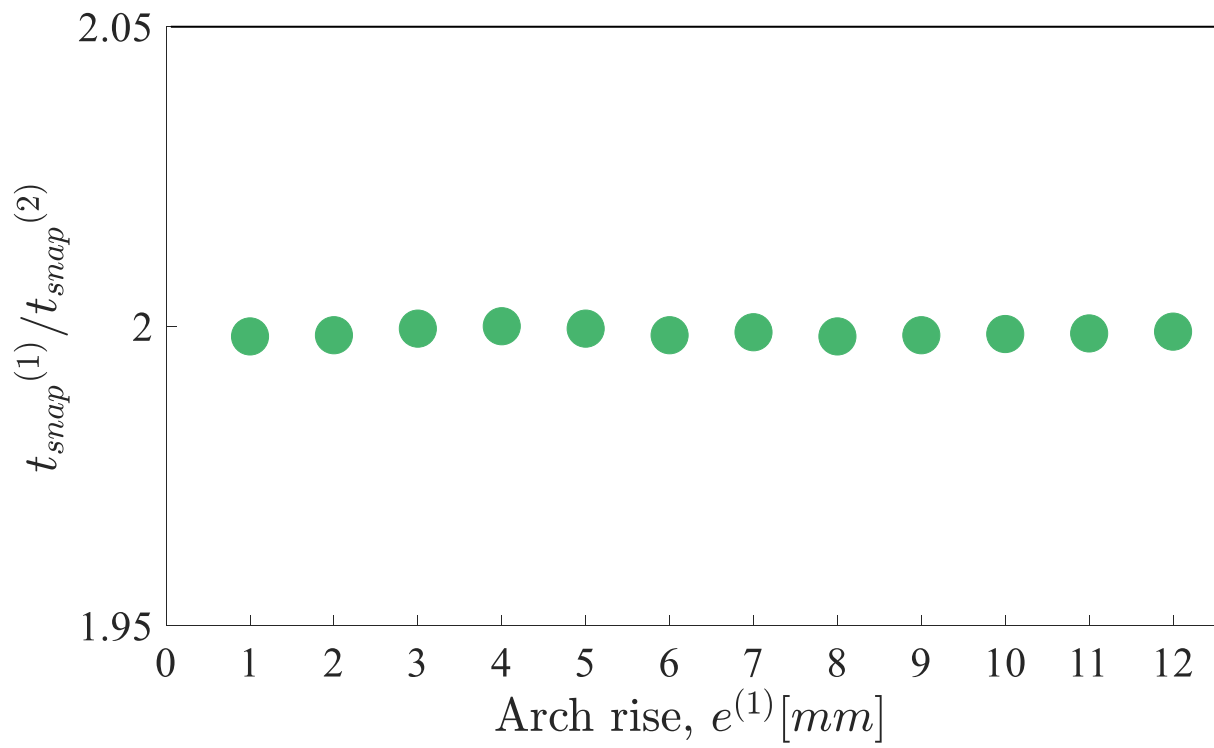


Figure S11: Ratio of snapping times (*i.e.*  $t_{snap}^{(1)}/t_{snap}^{(2)}$ ) with respect different arch rises for the plastically deformed shallow arches